



Cite this: *Nanoscale*, 2022, **14**, 9045

Theoretical modeling of ice lithography on amorphous solid water

Tao Liu,^a Xujie Tong,^a Shuoqiu Tian,^a Yuying Xie,^a Mingsai Zhu,^a Bo Feng,^a Xiaohang Pan,^a Rui Zheng,^{b,c} Shan Wu,^{b,c} Ding Zhao,^{b,c} Yifang Chen,^b Bingrui Lu *^a and Min Qiu *^{b,c}

Due to the perfection of the nanofabrication in nanotechnology and nanoscience, ice lithography (IL) by patterning ice thin-films with a focused electron beam, as a significant derivative technology of electron beam lithography (EBL), is attracting growing attention, evoked by its advantages over traditional EBL with respects of *in situ*-fabrication, high efficiency, high accuracy, limited proximity effect, three-dimensional (3D) profiling capability, etc. However, theoretical modeling of ice lithography for replicated profiles on the ice resist (amorphous solid water, ASW) has rarely been reported so far. As the result, the development of ice lithography still stays at the experimental stage. The shortage of modeling methods limits our insight into the ice lithography capability, as well as theoretical anticipations for future developments of this emerging technique. In this work, an e-beam induced etching ice model based on the Monte Carlo algorithm for point/line spread functions is established to calculate the replicated profiles of the resist by ice lithography. To testify the fidelity of the modeling method, systematic simulations of the ice lithography property under the processing parameters of the resist thickness, electron accelerating voltage and actual patterns are performed. Theoretical comparisons between the IL on ASW and the conventional EBL on polymethyl methacrylate (PMMA) show superior properties of IL over EBL in terms of the minimum feature size, the highest aspect ratio, 3D nanostructure/devices, etc. The success in developing a modeling method for ice lithography, as reported in this paper, offers a powerful tool in characterizing ice lithography up to the theoretical level and down to molecular scales.

Received 31st January 2022,
Accepted 30th May 2022

DOI: 10.1039/d2nr00594h
rsc.li/nanoscale

1. Introduction

Over the past few decades, electron beam lithography (EBL) as one of the powerful pattern generation techniques with high resolution, high alignment accuracy and high flexibility has achieved incredible successes in boosting the advances of pioneering science and cutting-edge technology in nanophotonics,^{1–4} nanoelectronics,^{5–7} nanobionics⁸ and bioscience,^{9–12} etc. However, the conventional EBL process on resists such as polymethyl methacrylate (PMMA) suffers from a number of daunting issues, such as the proximity effect, dense pattern collapse caused by surface tension in the developers,

low success yield of lift-off, toxicity of the chemicals used, etc. Because of this, nanoscale patterning for profiles with high aspect ratio, for example, is still extremely difficult. To break through the technical bottleneck, in recent years, e-beam lithography on water ice, *i.e.* amorphous solid water (ASW, H₂O),^{13,14} or organic ice such as anisole,¹⁵ alcohols¹⁶ and alkanes,¹⁷ nicknamed as ice lithography (IL) in general, has come to light. To carry out IL, the ice resists sprayed from a gas injecting system are condensed into the ice film on cryogenic samples. Various micro-nano patterns on either flat or non-flat surfaces through interactions of the electron beam with ice^{17–20} are first replicated without the necessity of a traditional developing procedure, directly followed by metallization in the same vacuum system. In the end, micro-nano structures/devices are fabricated when the samples are warmed up to room temperature. Compared with EBL, nanofabrication by IL possesses a number of unique advantages. First, it is a one-stop fabrication process in a vacuum without the need of multistep processes such as development and lift-off.¹⁴ Second, it is ecofriendly without the involvement of chemicals throughout the process.¹⁸ Third, the ice resist ASW contains much lighter elements, such as H and O elements,

^a*Nanolithography and Application Research Group, State Key Laboratory of ASIC and System, School of Information Science and Technology, Fudan University, Shanghai 200433, China. E-mail: yifangchen@fudan.edu.cn, lubingrui@fudan.edu.cn*

^b*Key Laboratory of 3D Micro/Nano Fabrication and Characterization of Zhejiang Province, School of Engineering, Westlake University, 18 Shilongshan Road, Hangzhou 310024, Zhejiang Province, China. E-mail: qiu_lab@westlake.edu.cn*

^c*Institute of Advanced Technology, Westlake Institute for Advanced Study, 18 Shilongshan Road, Hangzhou 310024, Zhejiang Province, China. E-mail: qiu_lab@westlake.edu.cn*

such that much narrower point spread functions should be expected in IL, giving rise to less proximity effect as well as smaller minimum feature size than that with PMMA in EBL. Fourth, water ice ASW elimination in IL is almost linear with the electron exposure dose,²¹ showing very low contrast of the ice resist, which is beneficial for three-dimensional (3D) profiling applications. Last but not least, attributed to the very low sensitivity of ice resists, IL is capable of high-precision *in situ* alignment¹⁹ such that IL-nanofabrication can be carried out on unusual substrates such as optical fibers,¹⁸ the probe tips of an atomic force microscope,²⁰ micro-cantilevers,²⁰ the grids of transmission electron microscopy,²⁰ suspended single-walled carbon nanotubes,^{19,20} etc. All of these advantages enable IL-nanofabrication to be an important supplement for traditional micro–nano-patterning technology.

Despite the significant developments achieved so far in IL-nanofabrication, the theoretical study of ice lithography on ASW has not yet been addressed owing to the lack of model regarding the fundamental principle of ice lithography, to the best of our knowledge. The shortage of modeling methods limits the in-depth understanding of ice lithography and the theoretical prediction for future developments of this emerging technology. So far, it has been reported that three effects may be involved in electron irradiation on ASW: local heating, sputtering or knock-on and ionization.^{22–25} The lithographic properties of ASW as a special e-beam resist have also been experimentally characterized by an in-house developed IL system based on a scanning electron microscope, including sensitivity, contrast, high-resolution linewidth, high-aspect-ratio nanostructures and dense lines.^{14,21} All the experimental achievements mentioned above have laid a solid foundation for the development of a theoretical modeling method.

In this work, a numerical simulation approach for calculating the e-beam exposure induced spatial charge distributions in ASW was developed for the first time, based on the Monte Carlo algorithm for the point spread functions. To simulate the lithographic profiles in ASW, which are represented by isoenergetic contours in resists, an e-beam induced etching ice model in the interactions between the kinetic electrons and the H₂O molecules was proposed. To test the fidelity of the modeling method, systematic simulations of ice lithography properties with the processing parameters of the resist thickness, the electron accelerating voltage and the patterns are performed.

Based on this approach, theoretical comparisons between the IL on ASW and the conventional EBL on PMMA have been conducted. The applications of the established modeling approach in computing a big variety of nanoscale profiles were demonstrated, including the electron loss energy density distribution of single pixel line exposure, the absorbing electron energy ability distribution (AEA) of 100 nm wide line exposures, X-ray Fresnel zone plates and 3D kinoform lenses, showing superior properties of IL over EBL in terms of the minimum feature size, the highest aspect ratio, 3D nanostructures/devices, etc. The success in developing the modeling method for ice lithography enabled us to characterize ice litho-

graphy up to the theoretical level and down to molecular scales for the first time and has filled the theoretical study gap in ice lithography as a whole, which will hopefully provide the IL-nanofabrication field with important guidance.

2. Simulations of ice lithography on ASW

2.1. Establishing the simulation approach

In general, the purpose of theoretical modeling of lithography is to quantitatively predict the profiles to be replicated in resists under certain lithographic conditions. Since the first commercialization of EBL in 1965, theoretical computing of EBL has been continuously developed and has reached a mature level. Typical examples of commercialized simulators for theoretical calculations of lithographic profiles include BEAMER for calculations of the exposure intensity distribution onto designed patterns, TRACER for calculations of spatial charge distributions in resists and LAB for simulating the development process of the exposed resists, supplied by GenISys Ltd. Almost all of the commercialized e-beam resists are included in the database nowadays, except for those in IL such as amorphous water ice and its counterparts. Also, the trajectories of primary electrons and energy distributions deposited in the resists are relevant to the e-beam energy, substrate materials, resist thickness and resist materials, such as the molecular structure, density and mean excitation energy.²⁶ This paper reports our progress in extending the application of the existing simulation method to ice lithography on ASW, enabling us to study the ice lithography properties in theoretical depth. Firstly, the resist parameters need to be imported into the TRACER database to define the properties of a new resist, including mass density, excitation energy and stoichiometry. Secondly, the simulation parameters of the physical model need to be set according to the actual process conditions in the TRACER software, such as the resist materials and thickness, substrate materials and thickness, e-beam energy, and number of electrons. Previous studies have reported that the energy loss of electron inelastic scattering can be calculated by the modified Bethe stopping power based on the continuous slowing down approximation method.²⁷ Based on the related Monte Carlo algorithm, the TRACER software can also calculate the electron trajectories and the electron loss energy density distributions (E^a) of single pixel lines with different resist thicknesses. Finally, the absorbing electron energy ability of the resist molecules (AEA, which is a qualitative and dimensionless value and has the same meaning as the electron loss energy density) can be achieved by the convolution of the exposure layout with the E^a (point/line spread function files) in the software, which can be considered as another form of E^a or the theoretical lithography profiles.

In this work, numerical calculations of ice lithography patterned profiles were carried out based on the established simulation approach, for the first time, using the existing BEAMER,

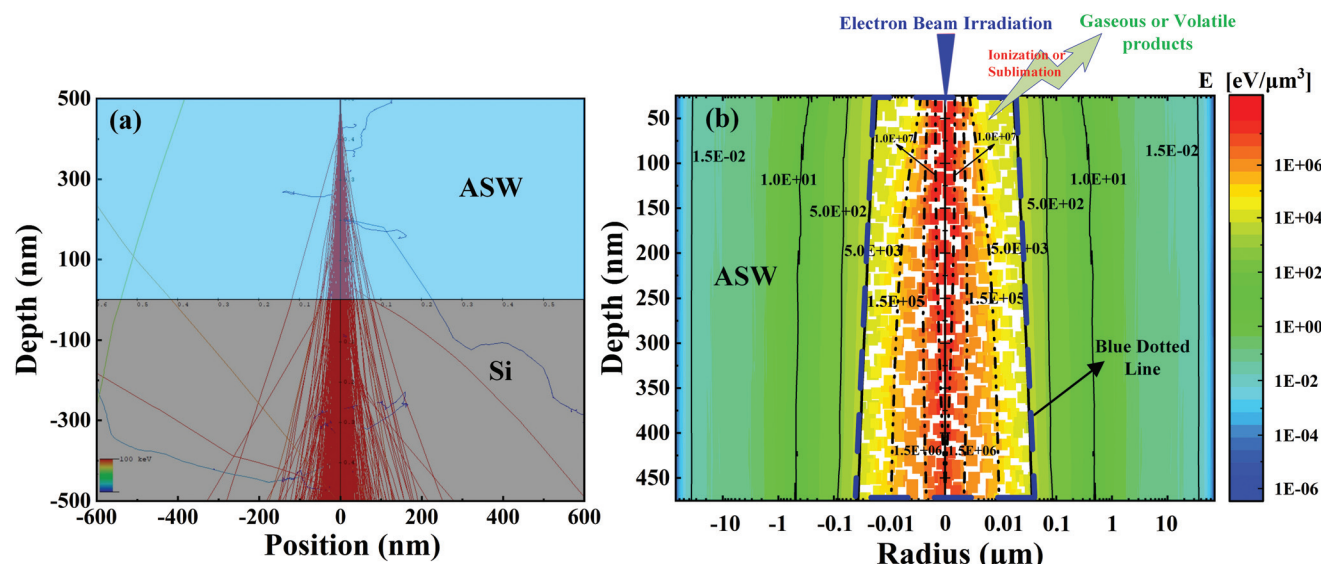


Fig. 1 The calculation results by our simulation approach for ice lithography. (a) The simulated trajectories of electrons in 480 nm thick ASW/Si with 10^6 incident electrons under the tension of 100 kV and (b) the electron loss energy density distribution (E^a) of single pixel line exposure.

TRACER and LAB software, delivered by GenISys Ltd. Fig. 1(a) presents the simulated trajectories by TRACER of 10^6 electrons with an ideal beam spot (*i.e.* the diameter is zero) at 100 kV accelerating voltage (AV = 100 kV) in 480 nm thick ASW on a Si substrate, in which the required simulation parameters (mass density: 0.93 g cm^{-3} , excitation energy: 75 eV, stoichiometry: H₂O) of ASW were adopted from the literature.^{28,29} Fig. 1(b) shows the energy distribution absorbed in ASW in space for the single pixel line exposure and the black lines represent the iso-energetic curves (E^a), *i.e.* the contours with constant energy density deposited in ASW. There is a decreasing gradient of the deposited energy density from the surface into the resist as usual. In conventional EBL, it is widely understood that the iso-energetic contours define the potential profiles of the

resist after development, depending on the sensitivity of the resist in EBL.

In ice lithography without the traditional developing process in developers, the proposed e-beam induced etching ice model is used to figure out the lithographic profiles. In this model, the kinetic energy of the focused e-beam is transferred to the ice through electron scattering with ASW molecules. The H₂O molecules are then ionized and sublimated directly to the vacuum after gaining sufficient energy from primary electrons, thereby becoming gaseous or volatile products. That is, ice lithography involves focused e-beam irradiation, energy transfer through electron scattering into ASW and a dry developing process. The threshold energy density essential to de-ice the ASW, which is on one of the iso-

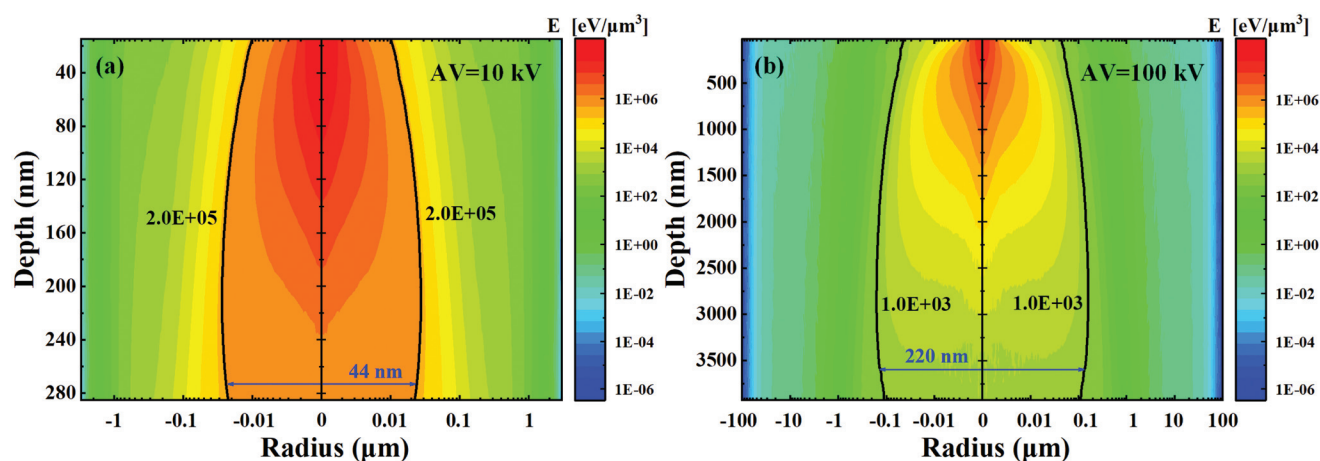


Fig. 2 Numerical simulation results of the electron loss energy density distributions (E^a) of the single pixel line exposure in (a) 290 nm thick ASW at 10 kV accelerating voltage and in (b) 4 μm thick ASW at 100 kV accelerating voltage, respectively, on Si substrate.

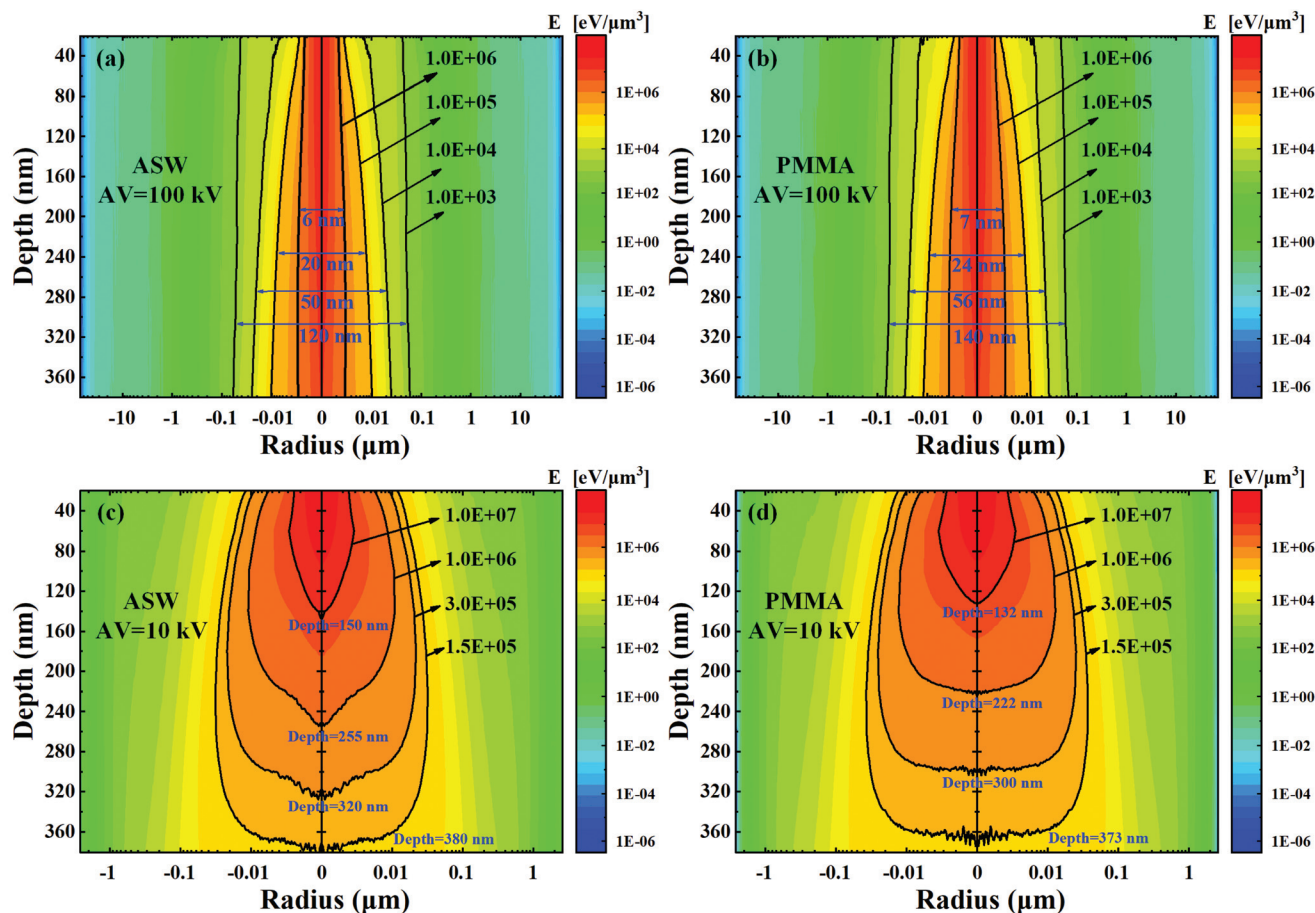


Fig. 3 The numerical simulation results of the electron loss energy density distributions (E^3) of the single pixel line exposure in (a) 380 nm ASW at 100 kV tension, (b) 380 nm PMMA at 100 kV tension, (c) 380 nm ASW at 10 kV tension and (d) 380 nm PMMA at 10 kV tension on Si substrate.

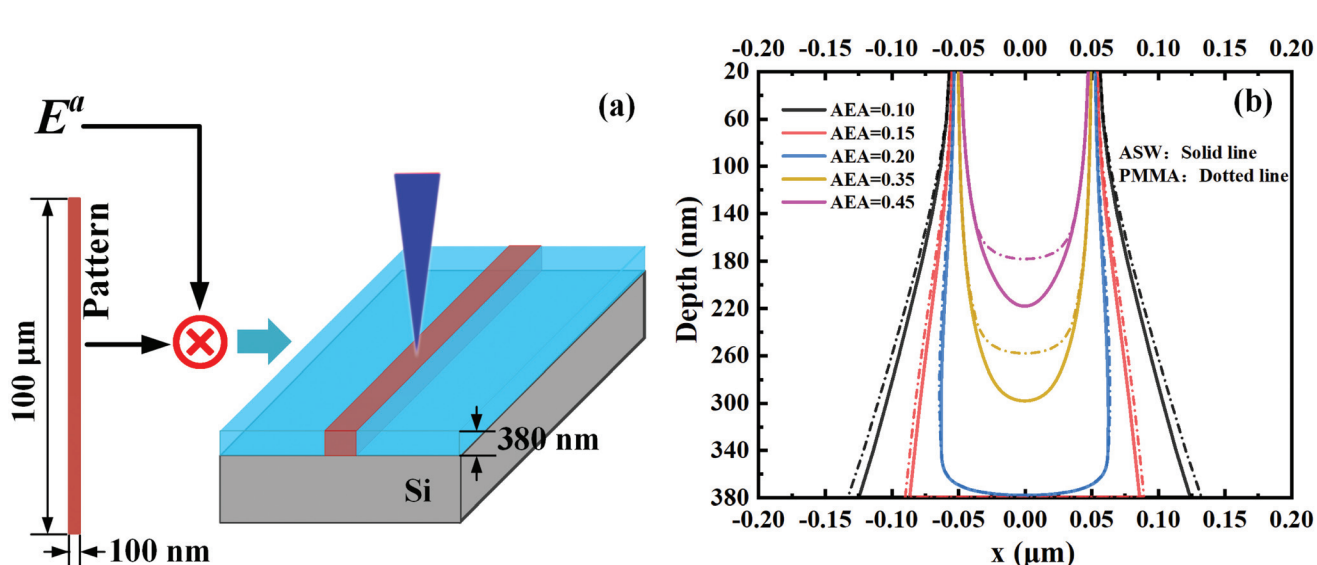


Fig. 4 The numerical calculation result of absorbing electron energy ability (AEA) in ice lithography. (a) Schematic of the convolution of the calculated electron loss energy density distributions E^3 with the exposed pattern. (b) The cross section of the AEA on a 100 nm wide line in 380 nm thick ASW at 10 kV tension on Si substrate.

energetic contours in Fig. 1(b), should be the ASW sensitivity. Any iso-energetic contours beyond the critical energy shall already be “de-iced”, forming the ice lithography patterns as shown in the blue dotted line area in Fig. 1(b). This model can be described by the formula,

$$P_{\text{Lithography}} = E_{\text{Total}}^{\text{a}} - \sum_{n=1} E_n^{\text{a}} (E_1^{\text{a}} < E_2^{\text{a}} < \dots < E_n^{\text{a}}) \quad (1)$$

where E_n^{a} is the resist-molecule absorbed iso-energetic curve, and E_1^{a} is the critical resist-molecule absorbed energy, which corresponds to the minimum exposure intensity required to pattern the ASW layer. $E_{\text{Total}}^{\text{a}}$ is the total electron energy inside the ice resist. $P_{\text{Lithography}}$ is the theoretically calculated profile, *i.e.* the area enclosed by iso-energetic contours with the threshold energy. Based on this model, like in conventional

EBL, the calculated contours in Fig. 1(b) should be the potential profiles of ice lithography, decided by the threshold energy density and the sensitivity.

2.2. Comparisons of the lithography performances between IL and EBL

Using TRACER, the spatial distribution of the electron loss energy through single pixel line exposure in 290 nm thick ASW coated on Si was first calculated by using 10^6 electrons in an ideal beam spot with 0 nm diameter at 10 kV, as presented in Fig. 2(a). The black color line corresponding to the iso-energetic contour at $E_1^{\text{a}} = 2.0 \times 10^5 \text{ eV } \mu\text{m}^{-3}$ shows the best feature as a trench. The aspect ratio of the patterned profile is about 6.5 : 1, in good agreement with the experimental results.²¹ For comparison, the ultimate aspect ratio of the trench by ice

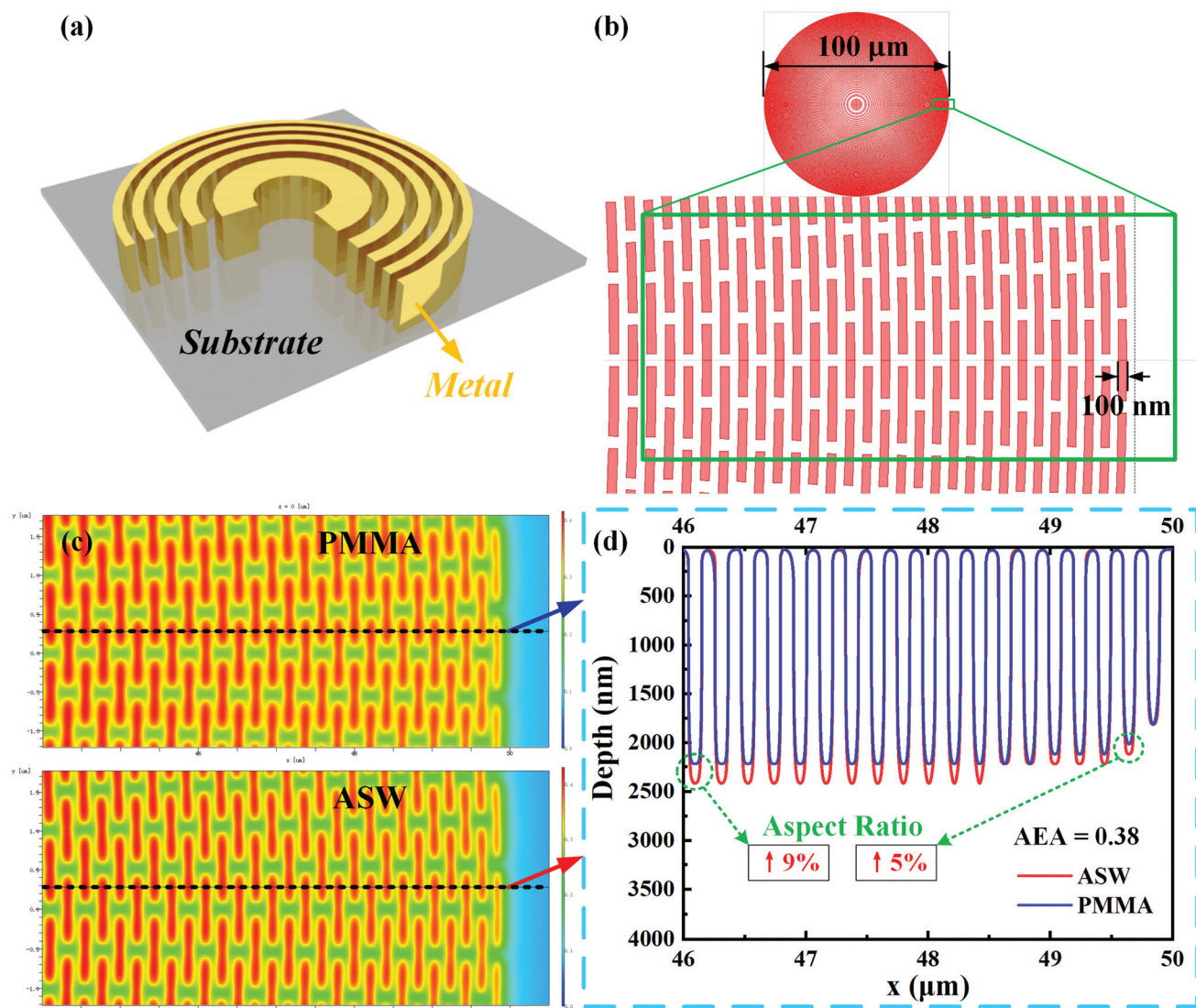


Fig. 5 Theoretical calculation results of the Fresnel zone plate profiles. (a) Schematic of the Fresnel zone plates. (b) The exposure pattern of a 100 nm resolution zone plate with a mechanically buttressed structure to prevent collapse. (c) Comparison of the AEA distributions in PMMA and in ASW at the resist depth of 2.125 μm. The total thickness is 4 μm. (d) The cross-section view of theoretically calculated profiles of the zone plate replicated in PMMA and in ASW when AEA is 0.38, under the same tension of 100 kV.

lithography at 100 kV was explored by simulating the replicated trench in 4 μm thick ASW using the single pixel line pattern. Fig. 2(b) shows that the iso-energetic contour at $E_1^a = 1.0 \times 10^3 \text{ eV } \mu\text{m}^{-3}$ should correspond to the most vertical profile, in which the ultimate aspect ratio of the exposure profile reaches 18 : 1. Obviously, higher acceleration energies give rise to higher aspect ratios as expected. Furthermore, the minimum line width in 380 nm thick ASW at 100 kV was explored, as shown in Fig. 3(a). The resolution and the aspect ratio of the ice lithography on ASW can reach 6 nm and 60 : 1 at $E_1^a = 1.0 \times 10^6 \text{ eV } \mu\text{m}^{-3}$, respectively.

E-beam lithography on ASW and on PMMA was theoretically compared as well. Fig. 3 presents the spatial distributions of deposited energy in both ASW and PMMA with the same thickness of 380 nm by an ideal e-beam spot with 0 nm diameter at 100 kV and 10 kV accelerating voltage, respectively. For the iso-energetic contours with the same deposited energy, the trench

width in ASW is narrower than in PMMA. The minimum trench width in ASW is 15% narrower than in PMMA at 100 kV (Fig. 3a and b). Comparing the iso-energetic curves between the ASW (Fig. 3c) and the PMMA (Fig. 3d) at 10 kV, all the trenches in ASW have narrower trench-widths and larger trench-depths than in PMMA for the same deposited energy E^a . The main reason lies in the lighter atoms (H and O) in ASW (H_2O) than those in PMMA ($(\text{C}_5\text{O}_2\text{H}_8)_n$). A higher density of larger atomic number atoms in resists leads to broader forward scattering, causing wider point spread functions as expected.

Fig. 4(a) schematically describes the convolution of the calculated point/line spread functions as described above, with the actual patterns, by using BEAMER software. For patterning the line of 100 nm in width and 100 μm in length by the e-beam of 10 nm in diameter at 10 kV accelerating voltage, the absorbing electron energy ability by the resist (AEA) for the

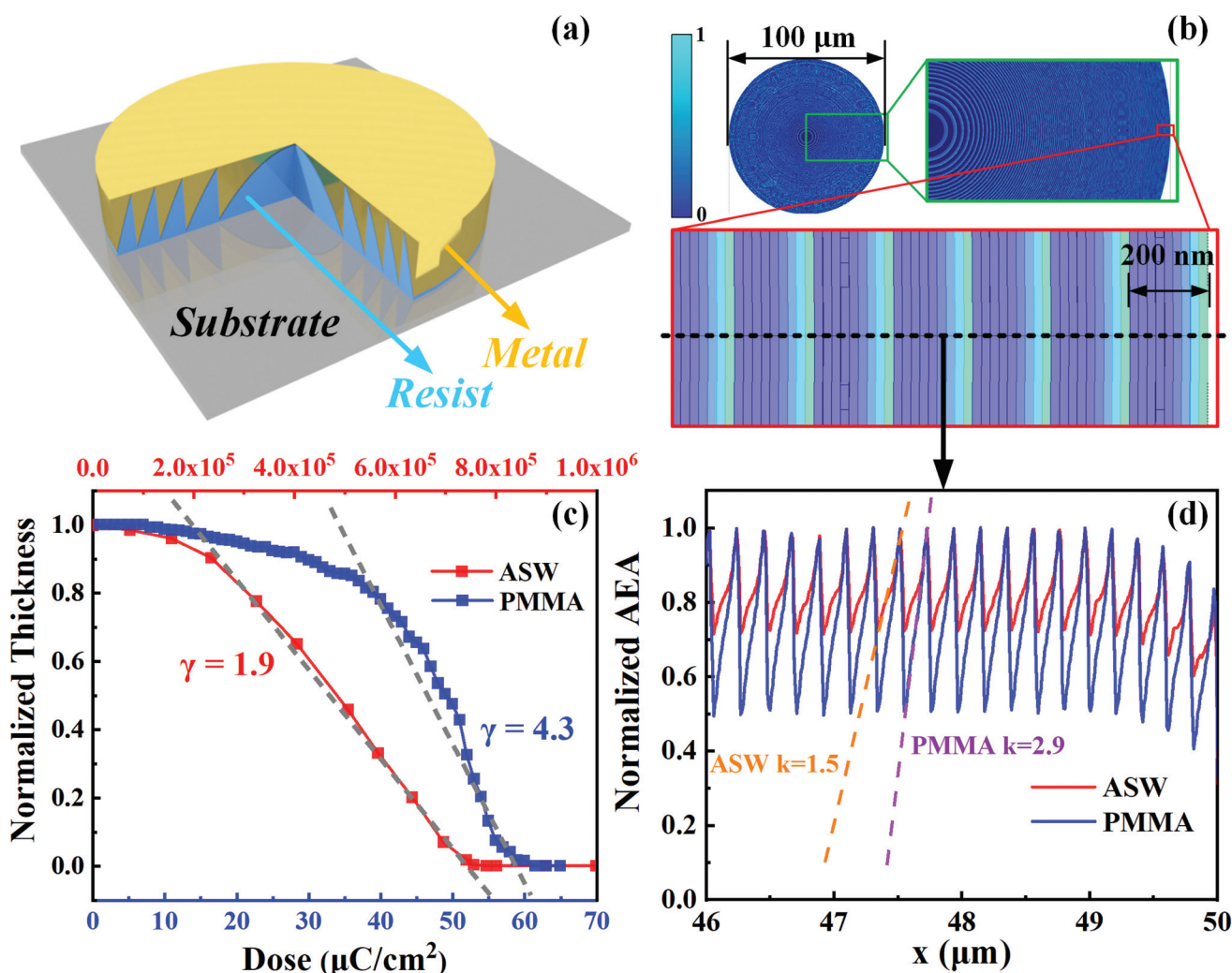


Fig. 6 Theoretical modeling results of the kinoform lens profile by ice lithography. (a) Schematic of the kinoform lens after the metallization process. (b) Schematic of the exposure dose pattern of the kinoform lens. (c) The normalized contrast curves²¹ for 190 nm thick ASW and 190 nm thick PMMA at 10 kV. (d) Comparison of the normalized AEA distributions of the kinoform zones in 190 nm thick ASW and in 190 nm thick PMMA. The base dose used for ASW is 0.8 C cm^{-2} and that for PMMA is $65 \mu\text{C cm}^{-2}$ under the same tension of 10 kV.

cross-section of the pattern line is presented in Fig. 4(b), where the resist thickness is 380 nm on a Si substrate. When AEA is in the high range from 0.35 to 0.45, the simulated aspect ratio of ASW is larger than that of PMMA. When AEA is in the low range from 0.1 to 0.15, the simulated minimum line-width of ASW is narrower than that of PMMA for the same reason as stated above.

2.3. The simulations of X-ray zone plate profiles

The calculated point/line spread functions in ice lithography have demonstrated superior performances over electron beam lithography thanks to the narrower forward scattering in ASW than in PMMA, arising from the relatively low atomic numbers of H₂O. The first benefit from the narrow point/line spread functions in IL is that the proximity effect, which limits the patterning resolution and the aspect ratio, is very much eliminated. Such an advantage becomes more significant when a high tension of 100 kV is applied in IL technology.

On the other hand, electron beam lithography, which seriously suffers from the proximity effect, is limited when replicating dense patterns like short-pitched gratings with ultra-high resolution well below 100 nm. A good example is when replicating Fresnel zone plates as diffractive lenses in X-ray optics,^{30,31} which need both high resolutions and high aspect ratios. In this paper, the patterning performance by IL was simulated and compared with EBL, trying to demonstrate the advantages of ice lithography.

Fig. 5(a) schematically illustrates the Fresnel zone plates with variable periods in the nanoscale and high aspect ratio for high resolution and high efficiency focusing/imaging. Fig. 5(b) shows the exposure pattern of a 100 nm zone plate without the proximity effect correction (PEC) to ensure that both IL-ASW and EBL-PMMA have the same exposure conditions in the simulation in this work. Based on the e-beam induced etching ice model, the AEA distributions in both PMMA and ASW are calculated by BEAMER with a 10 nm e-beam at 100 kV at the depth of 2.125 μm in the 4 μm thick resist, as presented in Fig. 5(c). The AEA of ASW has better-defined rectangular shapes than that of PMMA, meaning that the proximity effect in ASW is weaker than that in PMMA, and higher-resolution Fresnel zone plates may be achieved. Fig. 5(d) compares the cross-sectional profiles of a 100 nm zone plate in PMMA and in ASW, when AEA is 0.38. The results show that the aspect ratio of the inner rings and the outer rings by the IL-ASW can be increased by about 9% and 5%, respectively, compared with PMMA.

The low contrast of ASW is another advantage of applying ice lithography for 3D patterning of kinoform zone plate lenses with triangular profiles. Fig. 6(a) schematically illustrates the kinoform zone plate lens with a triangular structure, whose replication requires greyscale lithography. To achieve the kinoform shape of each zone, the exposure dose in each zone is divided into nine heights and each one is assigned by a certain amount of dose, as shown in Fig. 6(b). The contrasts [Fig. 6(c)] of both ASW²¹ and PMMA²¹ were imported into LAB software first when the resist thickness is 190 nm at 10 kV. The

contrast $\gamma^{15,21}$ of ASW is about 1.9, which is almost half of that of PMMA (4.3), indicating that ASW should be more adequate for 3D patterning than PMMA. In this simulation, the exposure base dose (sensitivity) of ASW and PMMA is set to 0.8 C cm⁻² and 65 μC cm⁻², respectively, according to Fig. 6(c). The normalized AEA distribution in the outer rings for the kinoform lens pattern was simulated by LAB with a 10 nm e-beam at 10 kV, as presented in Fig. 6(d). It is suggested that the zone slope in ASW is lower than that in PMMA, and ASW can optimize the AEA slope k of the outer ring by 48% compared with PMMA, indicating that ASW should have better quality in 3D patterning than PMMA.

3. Conclusions

This paper tackled the theoretical modeling of ice lithography by calculating the replicated profiles in ASW, using commercial software, BEAMER/TRACER/LAB, based on the Monte Carlo algorithm. The e-beam induced etching ice model has been proposed to explain the dry developing in ice lithography as a de-icing process in which H₂O sublimation from the ASW takes place under the e-beam irradiation. With this assumption, the lithography profiles in the resist, ASW, can be determined by the iso-energetic curves or the AEA distributions, following the same procedure as applied in the conventional electron beam lithography. Calculations of point/line spread functions of the electron loss energy density distribution in ASW first show superior properties of ice lithography over electron beam lithography in regard to the minimum linewidth and the ultimate aspect ratio, owing to less proximity effect in the former. The modeling of replicated profiles on both Fresnel zone plates and kinoform lenses also shows that ice lithography should give rise to better structural quality than electron beam lithography. Considering that ice lithography does not involve a wet developing process, the profile collapse due to the surface tension in the developer should never be a problem. Therefore, ice lithography as an emerging technology should find broad applications in 2D/3D patterning of nanodevices. The progress achieved in this work should be important in guiding IL development toward the manufacture of high-quality and high-complexity nanophotonics or electronic devices.

Author contributions

T. L., Y. C. and B. L. planned the projects and designed the modeling approach. T. L. and X. T. carried out the simulations of X-ray zone plate profiles. S. T., Y. X., M. Z., B. F. and X. P. provided guidance and advice on the use of the software. R. Z., S. W. and D. Z. provided the experimental data of ice lithography. T. L. carried out the simulations and data analysis. T. L. wrote and edited the paper. Y. C. and M. Q. initiated the research topic and supervised the whole research. All authors read and approved the final manuscript.

Conflicts of interest

There are no conflicts to declare.

Acknowledgements

This work is supported by the National Natural Science Foundation of China (NSFC: 61927820) and Shanghai Technology Innovation Center (Shanghai STCSM Projects: 19142202700).

Notes and references

- 1 F. M. Huang, T. S. Kao, V. A. Fedotov, Y. Chen and N. I. Zheludev, *Nano Lett.*, 2008, **8**, 2469–2472.
- 2 M. Khorasaninejad, W. T. Chen, R. C. Devlin, J. Oh, A. Y. Zhu and F. Capasso, *Science*, 2016, **352**, 1190–1194.
- 3 B. R. Lu, J. Deng, Q. Li, S. Zhang, J. Zhou, L. Zhou and Y. Chen, *Nanoscale*, 2018, **10**, 12378–12385.
- 4 X. Zou, G. Zheng, Q. Yuan, W. Zang, R. Chen, T. Li, L. Li, S. Wang, Z. Wang and S. Zhu, *PhotoniX*, 2020, **1**, 1–24.
- 5 Y. Chen, D. S. Macintyre, X. Cao, E. Boyd, D. Moran, H. McLellan, M. Holland, C. R. Stanley, I. Thayne and S. Thoms, *J. Vac. Sci. Technol., B: Microelectron. Nanometer Struct. – Process., Meas., Phenom.*, 2003, **21**, 3012–3016.
- 6 B. Feng, J. Zhu, B. Lu, F. Liu, L. Zhou and Y. Chen, *ACS Nano*, 2019, **13**, 8433–8441.
- 7 Y. Yao, L. Zhang, E. Orgiu and P. Samori, *Adv. Mater.*, 2019, **31**, 1900599.
- 8 S. Zhang, Y. Chen, B. Lu, J. Liu, J. Shao and C. Xu, *Nanoscale*, 2016, **8**, 9118–9127.
- 9 C. J. Bettinger, R. Langer and J. T. Borenstein, *Angew. Chem., Int. Ed.*, 2009, **48**, 5406–5415.
- 10 C. M. Kolodziej and H. D. Maynard, *Chem. Mater.*, 2012, **24**, 774–780.
- 11 B. Tian, J. Liu, T. Dvir, L. Jin, J. H. Tsui, Q. Qing, Z. Suo, R. Langer, D. S. Kohane and C. M. Lieber, *Nat. Mater.*, 2012, **11**, 986–994.
- 12 M. Lanniel, B. Lu, Y. Chen, S. Allen, L. Buttery, P. Williams, E. Huq and M. Alexander, *Thin Solid Films*, 2011, **519**, 2003–2010.
- 13 G. M. King, G. Schurmann, D. Branton and J. A. Golovchenko, *Nano Lett.*, 2005, **5**, 1157–1160.
- 14 Y. Hong, D. Zhao, D. Liu, B. Ma, G. Yao, Q. Li, A. Han and M. Qiu, *Nano Lett.*, 2018, **18**, 5036–5041.
- 15 D. Zhao, B. Chang and M. Beleggia, *ACS Appl. Mater. Interfaces*, 2020, **12**, 6436–6441.
- 16 W. Tiddi, A. Elsukova, H. T. Le, P. Liu, M. Beleggia and A. Han, *Nano Lett.*, 2017, **17**, 7886–7891.
- 17 D. Zhao, A. Han and M. Qiu, *Sci. Bull.*, 2019, **64**, 865–871.
- 18 Y. Hong, D. Zhao, J. Wang, J. Lu, G. Yao, D. Liu, H. Luo, Q. Li and M. Qiu, *Nano Lett.*, 2020, **20**, 8841–8846.
- 19 A. Han, D. Vlassarev, J. Wang, J. A. Golovchenko and D. Branton, *Nano Lett.*, 2010, **10**, 5056–5059.
- 20 A. Han, A. Kuan, J. Golovchenko and D. Branton, *Nano Lett.*, 2012, **12**, 1018–1021.
- 21 S. Wu, D. Zhao, G. Yao, Y. Hong and M. Qiu, *Appl. Surf. Sci.*, 2021, **539**, 148265.
- 22 N. G. Petrik and G. A. Kimmel, *Phys. Rev. Lett.*, 2003, **90**, 166102.
- 23 R. F. Egerton, P. Li and M. Malac, *Micron*, 2004, **35**, 399–409.
- 24 N. G. Petrik, A. G. Kavetsky and G. A. Kimmel, *J. Phys. Chem. B*, 2006, **110**, 2723–2731.
- 25 K. A. Gadallah, D. Marchione, S. P. Koehler and M. R. McCoustra, *Phys. Chem. Chem. Phys.*, 2017, **19**, 3349–3357.
- 26 N. Samoto and R. Shimizu, *J. Appl. Phys.*, 1983, **54**, 3855–3859.
- 27 D. C. Joy and S. Luo, *Scanning*, 1989, **11**, 176–181.
- 28 B. S. Befiand, D. E. Brown, M. A. Tolbert and S. M. George, *Geophys. Res. Lett.*, 1995, **22**, 3493–3496.
- 29 H. Bichsel and T. Hiraoka, *Nucl. Instrum. Methods Phys. Res., Sect. B*, 1992, 345–351.
- 30 J. Liu, J. Shao, S. Zhang, Y. Ma, N. Taksatorn, C. Mao, Y. Chen, B. Deng and T. Xiao, *Appl. Opt.*, 2015, **54**, 9630–9636.
- 31 S. Xie, J. Liu, S. Zhang and Y. Chen, *J. Micro/Nanolithogr., MEMS, MOEMS*, 2018, **17**, 043502.